Freeform injection molding of functional ceramics by hybrid additive manufacturing

Didilis, Kyriakos; Marani, Debora; Bihlet, Uffe; Haugen, Astri Bjørnetun; Esposito, Vincenzo

Published in:
Additive Manufacturing

Link to article, DOI:
10.1016/j.addma.2022.103197

Publication date:
2022

Document Version
Peer reviewed version

Freeform injection molding of functional ceramics by hybrid additive manufacturing

Kyriakos Didilis[a,b,*], Debora Marani[b], Uffe Bihlet[b], Astri Bjørnetun Haugen[a] and Vincenzo Esposito[a,*]

[a] Department of Energy Conversion and Storage, Technical University of Denmark, 2800 Kgs. Lyngby, Denmark

[b] Addifab ApS, Mårkærvej 2, 2630 Taastrup, Denmark

[*] Corresponding authors:

E-mail: vies@dtu.dk (Vincenzo Esposito) and kdi@addifab.com (Kyriakos Didilis)

Abstract

Freeform Injection Molding (FIM) is a hybrid manufacturing approach where 3D-printed sacrificial polymeric molds are used for Ceramic Injection Molding (CIM). This technique offers great additive manufacturing capabilities with shape complexity and material versatility. In this paper, we present a thorough analysis of the ability of FIM to process a variety of ceramic feedstocks and evaluate samples of different geometries with increasing geometrical complexity. The materials selected are zirconia, alumina and Pb-free piezoelectrics ($BaTiO_3$ and (Bi, Na)TiO_3 – $BaTiO_3$). Injection molding simulations are used to optimize the processing parameters. The quality of the fabricated ceramic parts is assessed by the microstructure, macro-defects, the geometrical features of the structural ceramics and the piezoelectric performance of $BaTiO_3$ and (Bi, Na)TiO_3 – $BaTiO_3$. The effect of green- and sintered-density, linear shrinkage (associated with sintering), and shape distortion are also discussed.

Keywords: Additive Manufacturing, Digital Light Processing, Ceramic Injection Molding, Functional Ceramics, Freeform Geometries, Piezoceramics

1. Introduction

The growing interest in ceramic materials for advanced applications has boosted the development of increasingly innovative materials and process-related techniques **[1, 2, 3, 4, 5]**, aiming to improve their performance, extend their functionality, and increase shape complexity. Outstanding examples are piezoelectric materials for sensors and acoustic wave transducers, actuators, and energy harvesting **[6]**. Functional ceramics are also applied within catalysis and energy **[7, 8]** or for their biocompatibility **[9],** thermal-mechanical properties **[10, 11]** and energy dissipation **[12]**. Although high-performance ceramics have been established in several key technological fields, traditional approaches are limited in processing complex geometries. The limits are often associated with thin parts weaknesses, and the high sintering temperatures used to consolidate the ceramics that can bring intense thermomechanical and residual stress.

Ceramic Injection Molding (CIM) is a well-established ceramic forming process capable of producing parts in complex shapes that find applications in numerous industries **[13]**. The method enables high production volumes, reproducibility and accuracy. The starting material, called feedstock, is a mixture of ceramic powders, thermoplastic binders and other additives. The feedstock is injected at high pressures and elevated temperatures into a two-component metallic mold forming the cavity. The mold opens upon melt cool-down, and the solid green parts are thus ejected. As a final step, the ceramic green part, characterized by low density and strength, undergoes the de-binding process, *i.e.,* removing the binder and organic additives and sintering for grain growth and densification. CIM suits high production volumes. However, mold machining metallic blocks are expensive and time-consuming, especially when advanced mold designs and components (cooling channels, inserts, retractable cores etc.) are required for complex shapes **[14]**. Customized parts and prototypes manufactured in low numbers are also cumbersome to manufacture. The emergence of Additive Manufacturing (AM) with numerous 3D-printing (3DP) methods has introduced novel possibilities for complex shapes while reducing waste **[15]**. Many AM processes for ceramic materials have been developed in the last few years **[16]**, including multi-material printing **[17]**. Such an evolution expands the range of applications **[18, 19, 20]** and designs **[21]**; some examples are heat management **[22, 23]**, photocatalysis **[24],** radio frequency communication **[25],** and structures with multi-functionalities **[26]**.

Stereolithography (SLA) and Digital Light Processing (DLP) of ceramics are based on the photopolymerization of ceramic slurries under a UV source. After printing, the green structures are de-binded and sintered to produce the final part. Normally the parts have acceptable roughness and can yield high densities. However, the reflective index of the powder can limit the ceramics that can

be processed **[14]**. Powder particles can influence the viscosity of the suspension **[27]**, and the curing depth (and profile) changes with the energy source **[28].** The ceramic slurry is a suspension where particle segregation can occur between the printed layers **[29]**. Powder-bed processes can either sinter the powder-part layers directly from the high-energy laser or spray a binder on the powder to form the layers and build the green part.

Similarly, powder characteristics, such as morphology and size, affect the flow and spread on the powder bed **[30]**. In addition, the energy source-powder interaction and heat absorption can introduce thermal stresses **[31]**. Any resulting defects will lower the density significantly **[32]**, with the indirect methods performing better on this aspect.

The extrusion-based processes (e.g., Fused Deposition Modeling (FDM)) are based on thermal energy to melt the binder contained in the ceramic paste/filament and fuse the deposited layers. The filament can have high solid contents with reduced shrinkage at the sintering step. However, rheology is key, and nozzle clogging is the most common issue in FDM, affecting particle/additive dispersion in the paste when applicable **[29]**. Other processes that use pastes or inks, with more advanced material delivery systems, *e.g.*, Direct Ink Writing (DIW) processes **[33, 34]**, require lower solid content to allow material flow through smaller diameter nozzles or syringes. Drying or curing the deposited material must occur before depositing the following layers to avoid collapsing the green structure (limiting the height and overhang features). Low density and shrinkage are expected due to low solid loading in the ink formulation **[32]**. Regardless of the process and the material type, inter-layer defects could be introduced, and there is a chance that they will be periodically repeated in the entire structure. This process requires extensive material preparation steps for the formulation and characterization, followed by experimentation on the relevant curing parameters. Such requirements can increase complexity, especially at the early stages of product development or research activities, where switching to other materials and design iterations are frequently required.

The benefits of AM can be used in conjunction with other conventional processes like CIM to produce complex shapes with a more sustainable and robust process. Early work on hybrid processes reported sacrificial photopolymer molds that can be thermally decomposed **[35]** or dissolved in alkaline solution **[36]**, water **[37]** or acetone **[38]**. State-of-the-art methods have produced structures with finer features **[39]**, **[40]**, **[41]**. However, the above examples use gel-casting or molding at low temperatures and pressures and require significant time to cure the ceramic formulation.

In this paper, we combine CIM and AM into one hybrid process called Freeform Injection Molding (FIM). The method exploits the benefits of both AM and CIM. A photopolymer material formulation

is 3D-printed into a sacrificial thermosetting mold. After CIM, the mold is chemically dissolved, yielding the geometrical capabilities and waste savings of 3DP combined with IM's material versatility and forming characteristics.

The sustainable aspect of FIM is attractive in applications such as prototyping, replacement or customized parts **[42, 43, 44]**. The high potential of FIM applied in Powder Injection Molding relies upon the resolution of the geometrical features and on surface smoothness **[45, 46]**. Recently, Wick-Joliat et al. **[47]** also incorporated a dissolvable mold in CIM to produce complex geometries with the desired physical properties. In earlier work, we also explored the impact of different binder systems and particle distribution in ceramic feedstock formulations, focusing on melt flow characteristics, binder distribution, and relevant defects **[48]**. Despite the benefits and geometrical capabilities demonstrated by adopting sacrificial 3D-printed molds in different systems, important issues must be addressed, especially when increasing feature resolution and geometrical complexity.

We conduct critical analysis, including strategies for the gate positions, processing and modelling to produce finer geometries and prevent defects. We propose a set of analytical tools, *e.g.*, suitable characterization techniques (CT scanning and volumetric deviation in the sintered materials), to relate 3D structures and inner defects with the processing steps. We also selected several functional ceramics processed into complex geometries. Curved surfaces (lens, dome) and periodic/freeform features (cylindrical lattice / double helix) were fabricated with yttria-stabilized zirconia (ZrO_2 with 3 mol% Y_2O_3, 3Y-TZP) and alumina (Al_2O_3) commercial feedstocks respectively. Powders of the lead-free piezoelectrics barium titanate ($BaTiO_3$, BTO) and bismuth sodium barium titanate ($(Bi, Na)TiO_3$ - $BaTiO_3$, BNT-BT) were also compounded into feedstocks. The quality of the ceramic parts was assessed using a set of descriptors defining features such as microstructure and macro-defects, linear shrinkage, density, shape distortion, and the functional properties of the piezoelectric materials.

2. Materials and methods

2.1 Materials

The photocurable resin used to print the molds was IM 2.0 Special 1 (Addifab, Denmark), a commercial product developed specifically to enable FIM. This reactant is an acrylic resin prepared with an acryloyl monomer and a multifunctional acrylate with a type I photo-initiator (<1 % diphenyl (2,4,6- trimethyl benzoyl)phosphine oxide). Isopropyl alcohol (IPA) 99.9% (Borup Kemi I/S) was used

to clean the molds after printing. Sodium hydroxide pellets (Borup Kemi I/S) were used to prepare the de-molding alkaline aqueous solution (DI water).

For the injection molding of ZrO_2 with 3mol% Y_2O_3 (3Y-TZP), we used a commercial feedstock (INMAFEED K3012, INMATEC Technologies GmbH) with a polyoxymethylene (POM) based binder system and a powder content of 80 - 85 wt.% (corresponding to 50 - 60 in vol%). The Al_2O_3 commercial feedstock (INMAFEED K1010, INMATEC Technologies GmbH) with polyethylene glycol (PEG) based binder and a powder content of 80 - 85 wt.% (50 - 60 in vol%). The $BaTiO_3$ feedstock was compounded at Fraunhofer IKTS, Germany, from 83.5 wt.% BTO powder (55 in vol%) (Alfa Aesar) in a POM-based proprietary binder system. The BNT - BT feedstock was compounded at DTU Energy, Denmark, from 84 wt.% BNT-BT powder (45 in vol %, provided by MEGGITT A/S) in ethylene-vinyl acetate (EVA) and wax binder system.

2.2 Processing of FIM molds and ceramic feedstocks

The FIM process steps are summarized in **Fig. 1,** starting from the CAD model of the part to the final sintered ceramic structure. The CAD models of the FIM molds were designed with SOLIDWORKS (Dassault Systems) and exported as STL files. Subsequently, they were "sliced" with the AddLine Manager software (Addifab) at a layer thickness of 100 µm. For the given layer thickness and IM 2.0 Special 1 (Addifab) resin material, the UV intensity of the projector was set to 20%, and the exposure time was 1.8 s. The single cavity molds were printed with an AFU5 AddLine DLP printer (Addifab) with a projector resolution of 1920 x 1080 pixels and an LED wavelength of 365 nm.

After printing, the FIM molds were cleaned using the PFU2 Cleaning Station (Addifab), which incorporates three sequential cleaning steps with IPA (10 minutes in each step) to ensure that unreacted resin is flushed out of the narrow channels in the mold cavity. The molds were then post-cured using an Ottoflash UV flasher (Envistiontech) with 2000 flashes (10 flashes per second) on each side of the mold to ensure that the samples were free of unreacted resin.

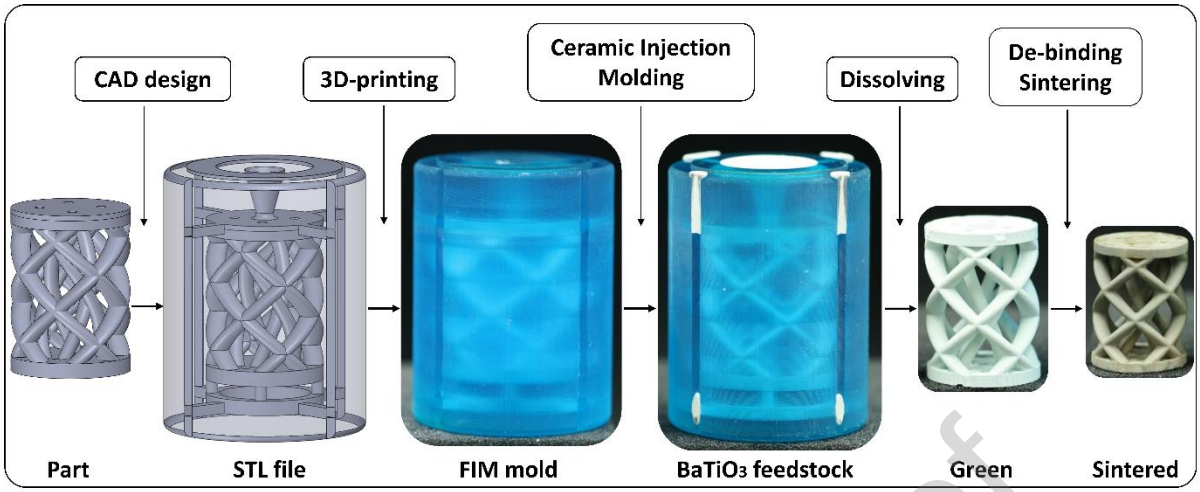

Fig. 1: The FIM process steps exemplified by fabricating a ceramic double helix ($BaTiO_3$). The CAD model of the part and the design of the FIM mold before it is 3D-printed, injection-molded and dissolved, and finally, de-binding and sintering of the ceramic part.

Simulations were carried out with Moldex 3D (Moldex3D) to define a process parameters window for the experimental feedstocks. POM_UltraformN2720M63 was used from the material library for the BTO double helix samples and EVA_EvatheneUE630_1 for the BNT-BT lens. The filling analysis was carried out using a steel mold. The effect of increased injection temperature, packing pressure, and time on the shear stresses and resulting defects was studied on the actual green parts. In addition, the simulations examined the optimum location and size of the gate and outlets on the molds to investigate melt filling and temperature profile across the double helix cavity. As a result of the simulation, an increase in the suggested/nominal injection parameters was used to improve melt front fusion. Specifically, the injection temperature was increased by 10 - 15°C (across the injection screw zones), the injection pressure was increased to 850 bar, and the packing pressure and time were increased to 700 bar and 10 s, respectively.

The ceramic feedstocks were injected using a BOY 22 A PRO injection molding machine (BOY Machines, Inc.). The feedstocks were processed according to the material database information in the simulation software, in a temperature range 10 - 15°C higher than the nominal. **Table 1** reports the injection molding parameters in detail. The BTO was molded at higher temperatures in the injection nozzle (200°C) to aid the injection and melt front fusion. The final de-molding step of the FIM process was carried out using the PFU3 Demolding Station (Addifab). The molds were dissolved in a highly alkaline solution (aqueous NaOH, 1 M) at 50°C.

The parts were de-binded and sintered in air with Nabertherm muffle furnaces (Nabertherm GmbH). The experimental details are described in **Table 1**. The de-binding treatment parameters for the two

BNT-BT and BTO feedstocks were selected based on TG-DTA analysis of the feedstocks (not shown here) to determine the exact decomposition temperatures of the organic binders.

Table 1. The injection molding parameters for the ceramic feedstocks and the de-binding/sintering conditions.

Material	Temperature at screw (°C)	Temperature at nozzle (°C)	Injection speed (ccm/s)	Injection pressure (bar)	Packing pressure (bar)	Packing Time (s)
3Y-TZP	185	195	25	500	350	3
Al_2O_3	150	165	35	750	450	3
BTO	185	200	25	850	700	10
BNT-BT	160	175	13	750	700	6

	De-binding Temperature (°C)	Heating Rate (°C/h)	Holding time (h)	Sintering Temperature (°C)	Heating Rate (°C/h)	Holding time (h)
3Y-TZP	600	15	2	1500	60	4
Al_2O_3	300	15	2	1680	60	4
BTO	250	10	2	1300	30	4
	400	10	2			
BNT-BT	250	10	2	1140	30	3
	400	10	2			

2.3 Characterization of fabricated parts

Scanning Electron Microscopy (SEM) was used to evaluate the microstructure of the samples with a TM 3000 tabletop microscope (Hitachi High-Technologies Corporation). Samples were fractured to evaluate the grain characteristics and polished to 1 µm to observe the porosity. The grain diameter was measured using ImageJ **[49]**.

Computed tomography (CT) was carried out on an XT H 225 Industrial CT scanner (NIKON), at 220 kW, 10 W, with a pixel size of 19.7 µm. The CT data were analyzed with Avizo Lite (Thermo Fisher Scientific Inc.) to reconstruct the scanned volume and evaluate the internal defects in different plane orientations.

Density was measured with the Archimedes principle in DI water, using an XS204 Excellence Analytical Balance, scale and density kit (METTLER TOLEDO). The relative density was calculated based on the crystallographic density of the ceramic powder included in each feedstock. The dimensions of green and sintered parts were measured with a calliper to calculate linear shrinkage after the final sintering step.

Shape distortion of the three different sintered geometries was conducted with digital models derived from CT scans and GOM Inspect (GOM GmbH). The CT data were imported as mesh bodies and compared to the actual parts' CAD models, considering the calculated linear shrinkage measured

on the sintered parts. The models were aligned with the CAD model scaled down by the size factor in each case, derived from the ratio of green/sintered dimensions measured on the actual parts to match the structure height and diameter of the sintered part.

The piezoelectric testing was carried out with a TF 1000 Analyzer (aixACCT Systems GmbH). The samples for piezoelectric characterization were coated with a thin layer of silver conductive paint (SPI Supplies Division Structure Probe, Inc.). For the evaluation of the electromechanical performance, a triangular electric waveform was applied at a frequency of 1 Hz at room temperature. The electric field was applied in 10 V increments for BTO, up to 2.57 kV/mm, and at 350 V increments for BNT-BT, up to 7 kV/mm. Poling was carried out only on BTO with an electric field of 2.0 kV/mm as the material cooled down from 135°C to room temperature after the piezoelectric measurement. The longitudinal piezoelectric charge coefficient, d_{33}, was measured with a Berlincourt d_{33} meter (APC International) after the piezoelectric measurement of BNT-BT and after the poling process of BTO.

3. Results and discussion

We analyze the FIM process by exploring geometrical complexity and highlighting critical issues and strengths of the method. The geometrical features entail many parameters associated with microstructural features, defects generated by internal stresses, shape distortions, and surface quality of the parts with different dimensions.

3.1 Microstructure and defects in simple 3D geometries: lenses

The analysis of the microstructural features in simple 3D geometries such as curved surfaces, lenses and domes are representative of samples that do not interpenetrate the mold. The minimal interface coupling aids the dissolving process, aiming to reduce any likely damage.

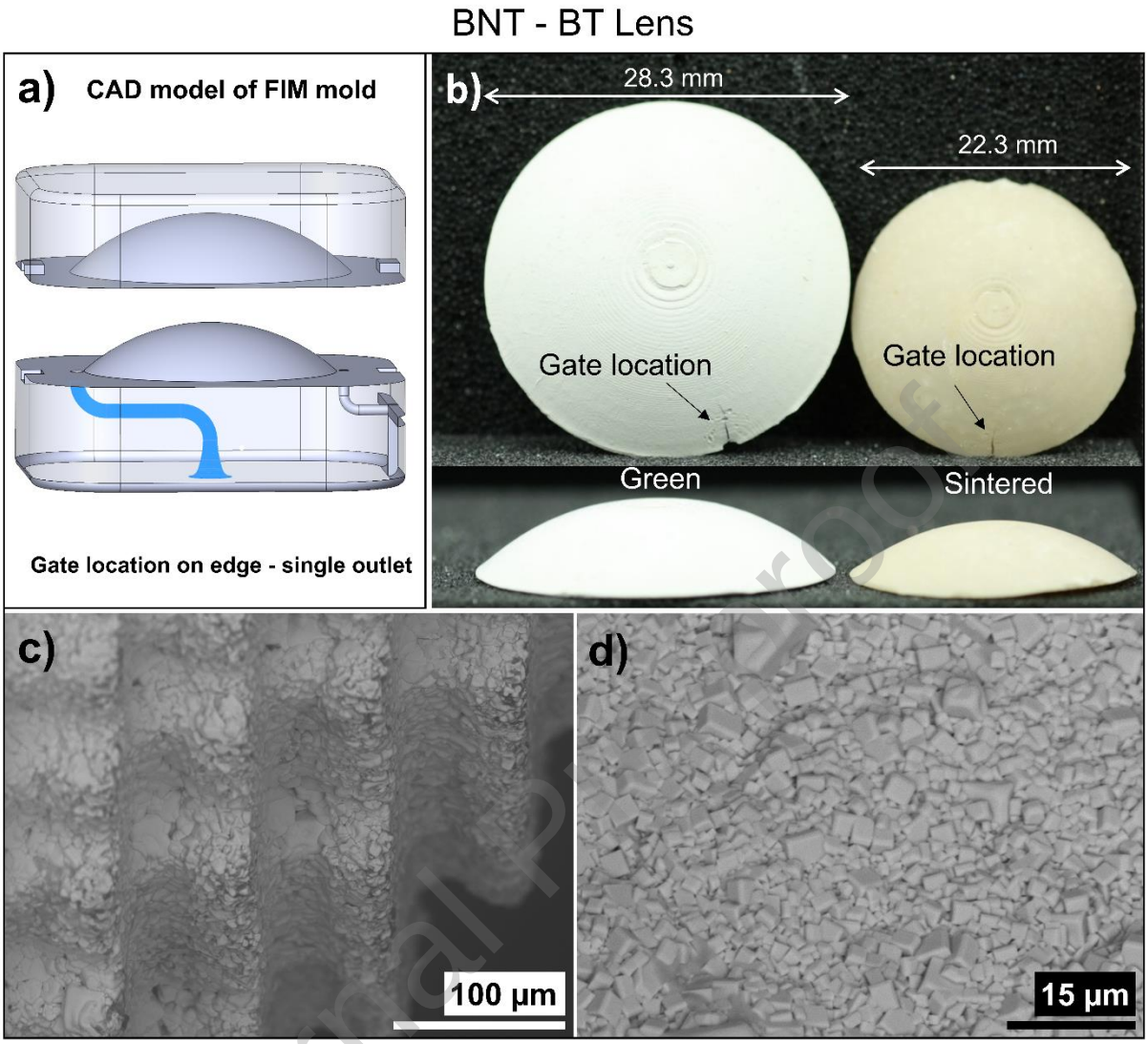

Fig. 2: a) The CAD model of the FIM split mold with the gate located on the edge of the lens rim. The BNT-BT feedstock shaped into the b) green and sintered lens geometries, c) the FIM mold resolution after grain growth on the sintered surface, and d) the resulting grains after sintering on a fractured cross-section.

Fig. 2 shows the BNT-BT lens feedstock, with the gate and outlet located on the two edges of the lens (**Fig. 2a**), on the same side of the FIM split mold. The top half of the split mold was removed after injection, and only the bottom section containing the green part was dissolved. The process was effective, except for the thin edge regions where small cracks formed around the gate during the resin dissolution (**Fig. 2b**). This defect was attributed to residual stresses during feedstock cool-down **[50, 51]** and stress from the expanding mold during dissolving. The cracks were located only around the gate and not the outlet. The gate size (Ø 1.4 mm) was fitted with small margins concerning the thickness of the lens edge (1.45 mm). For the outlet, the smaller diameter (Ø 1.0 mm) than the lens rim was the weaker point that cracked during dissolving without damaging the

lens. This result points out the critical role of the green part strength that, for the thinner regions, are susceptible to damage during mold dissolution.

Although the high content of organic compounds in the BNT-BT feedstock (55 vol%), the SEM observations did not reveal any large pores, cracks, or excessive distortion that are typical defects expected after de-binding **[52]**. The microstructure appeared homogenous with a few gaps between the grains at the surface (**Fig. 2c**), and visible step-like features originated from the 3D-printed mold and the layered curvature. We observed a dense microstructure (**Fig. 2d**) with average grain sizes of 3.4 µm and 1.7 µm for the medium and small grains, respectively. Only a few larger and smaller grains outside this range were observed.

The FIM mold was designed with an updated gate/outlet system to avoid residual stress issues. **Fig. 3** shows the 3Y-TZP lens and domes. For this split mold design, the gate was placed on the top of the curvature, and multiple outlets were on the bottom (**Fig. 3a** and **d**). This configuration allows a uniform feedstock distribution in the injection and then relaxes the stress observed in the lateral mold design. The 3Y-TZP lens (**Fig. 3b**) and dome (**Fig. 3e**) maintained their shape without defects in the green and sintered state after all the processing steps (see **Table 1**).

Fig. 3c shows residual and isolated porosity on a polished lens cross-section, probably due to binder residual in the green body. The grain size measured is comparable to the values reported in the literature **[53, 54]**, using similar starting particle sizes (80 µm and 13 nm), where an increment of grain growth was observed at increasing sintering times and temperatures.

Fig. 3c shows a wave pattern on the sintered surface with feature sizes corresponding to the print resolution. Notably, the surface of the sintered part does not exhibit any cracks or delamination defects in the core of the piece between the layers. Delamination at the layers is a common defect in 3D-printed structures due to insufficient inter-layer adhesion and thermal effects **[32]**. Thus, the ceramic feedstock can imprint the shape of the 3D-printed mold and retain it during grain growth, suggesting a stable sintering behavior (both in the lens and in the dome). The same features were observed on the BNT-BT lens (**Fig.2 c**). The micrograph of the fractured section (**Fig. 3f**) suggests a dense microstructure consisting of homogeneous 3Y-TZP grains with a size of 0.5 - 0.9 µm.

In conclusion, simple 3D shapes of curved geometries can be fabricated by simple split molds preserving their shape. De-molding defects on terminal sections' gate/outlet system were solved with an updated gate/outlet design. No defects were observed on the critical mold inter-layer regions after sintering, regardless of the de-molding issues.

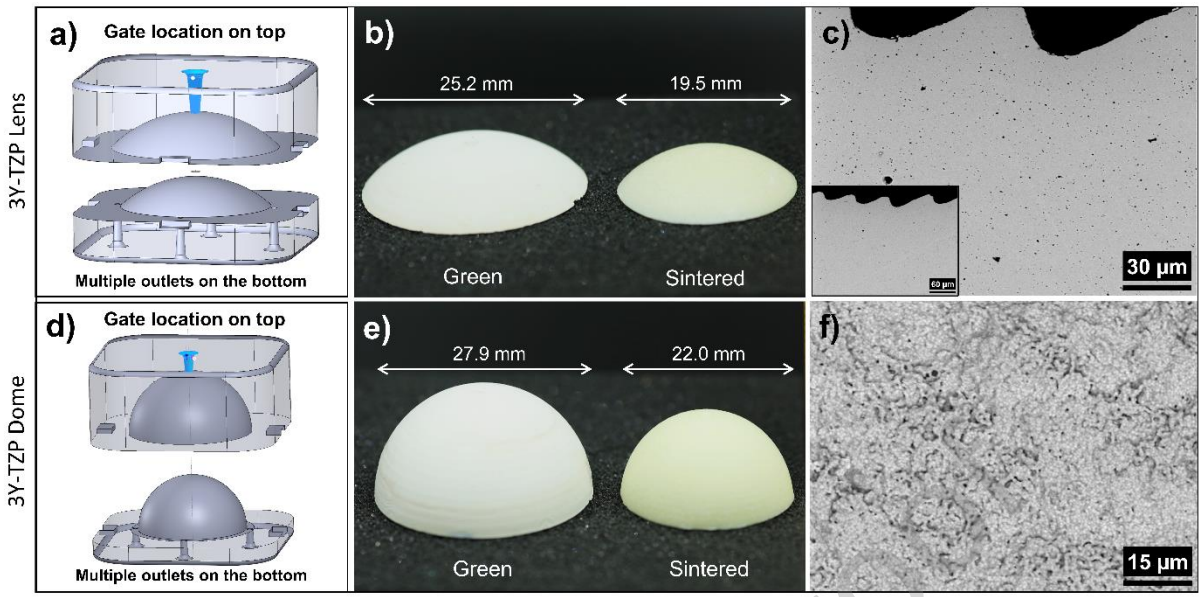

Fig. 3: The CAD models of the FIM split molds with the gate located on the top center of the curvature for a) the lens and d) the dome geometry). Green and sintered ceramic bodies for the 3Y - TZP b) lens and e) dome. SEM images of a fractured section after sintering revealing c) the degree of porosity on a polished sample at x1000 magnification and f) the grains on a fractured section at x2000 magnification.

3.2 Microstructure and defects in complex 3D geometries: double helix

Moving from the split molds and the mitigation of cracks by updating the gate design, we explored how purely freeform geometries respond to a sacrificial single cavity mold by full dissolution. The geometrical complexity is represented by the 3D structure called the "double helix" (**Fig. 4**). This shape is endowed with freeform geometrical features, thickness variation, and a change in melt flow direction **[48]**. The shape consists of a cylindrical lattice incorporating two internal helixes. Contrary to the lenses, the mold and the samples were interpenetrated and could not be split.

Fig. 4 shows the double helix geometry fabricated in Al_2O_3 from a PEG-based feedstock (**Fig. 4a**) and BTO from a POM-based feedstock (**Fig. 4b**). The supplier's recommended injection molding parameters for the Al_2O_3 feedstock formulation were used, and the mold appeared filled after the injection. The single cavity FIM mold was dissolved, and towards the end of this step, cracks on the X-section of the lattice junctions appeared, where the melt fronts met during the injection. The cracks on the green part are shown in **Fig. 4a**. After the de-binding and sintering process, these defects were also observed in the sintered part (highlighted in **Fig. 4a**). Blisters associated with excessive binder vapors were also visible by the naked eye. The CT scan on the Al_2O_3 double helix in **Fig. 4b** also reveals internal delamination defects. Therefore, in addition to the cracks observed on

the green state (after injection and de-molding), the section views reveal defects that originated during de-binding.

This result highlights that a balance between mold expansion and green part strength is critical for defect-free geometries. Selecting a stronger binder in the feedstock is a possible solution to provide more strength for the green parts. However, adjusting the injection parameters to the geometry of the cavity allows an optimized flow and can be used to maintain the feedstock materials. Flow optimization significantly reduced the number and size of the lattice junction point's cracks. At the same time, the green BTO sample appeared nearly defect-free after dissolving the mold (**Fig. 4c**). Yet, the reconstructed volume of the sintered BTO double helix after the CT scan in **Fig. 4d** shows that the cracks on the lattice junction were reduced. The CT scan views from the top and side (**Fig. 4d**) revealed minor cracks at the lattice junction and significantly reduced de-binding defects. No delamination defects appeared in the BTO feedstock, suggesting a better overall performance for the binder during mold dissolving and de-binding. The sintering performance did not show any unexpected effects (the microstructure of the BTO samples after sintering is shown in **Fig. 6**).

The melt flow and packing were further improved by adjusting the outlet design on the mold before injection. Removing the top outlets from the FIM mold was chosen to minimize pressure losses at the top section of the double helix and instead guide the melt towards the end of the cavity and flow out only from the bottom outlets. Following injection molding with the updated outlet system, the green part did not crack at the critical X-junction points after dissolving (**Fig. 4f**). The fusion of the melt fronts improved to the point by rounding off the X-junctions (see dashed line in **Fig. 4f**). This change reduced the stress concentration significantly at these critical points of the green part that are susceptible to cracks (**Fig. 4e**) during the dissolving of the FIM mold. The conclusion is that adopting a design change on the 3D-printed FIM mold of complex shapes can critically reduce the defects derived from the green parts' injection molding and dissolving process.

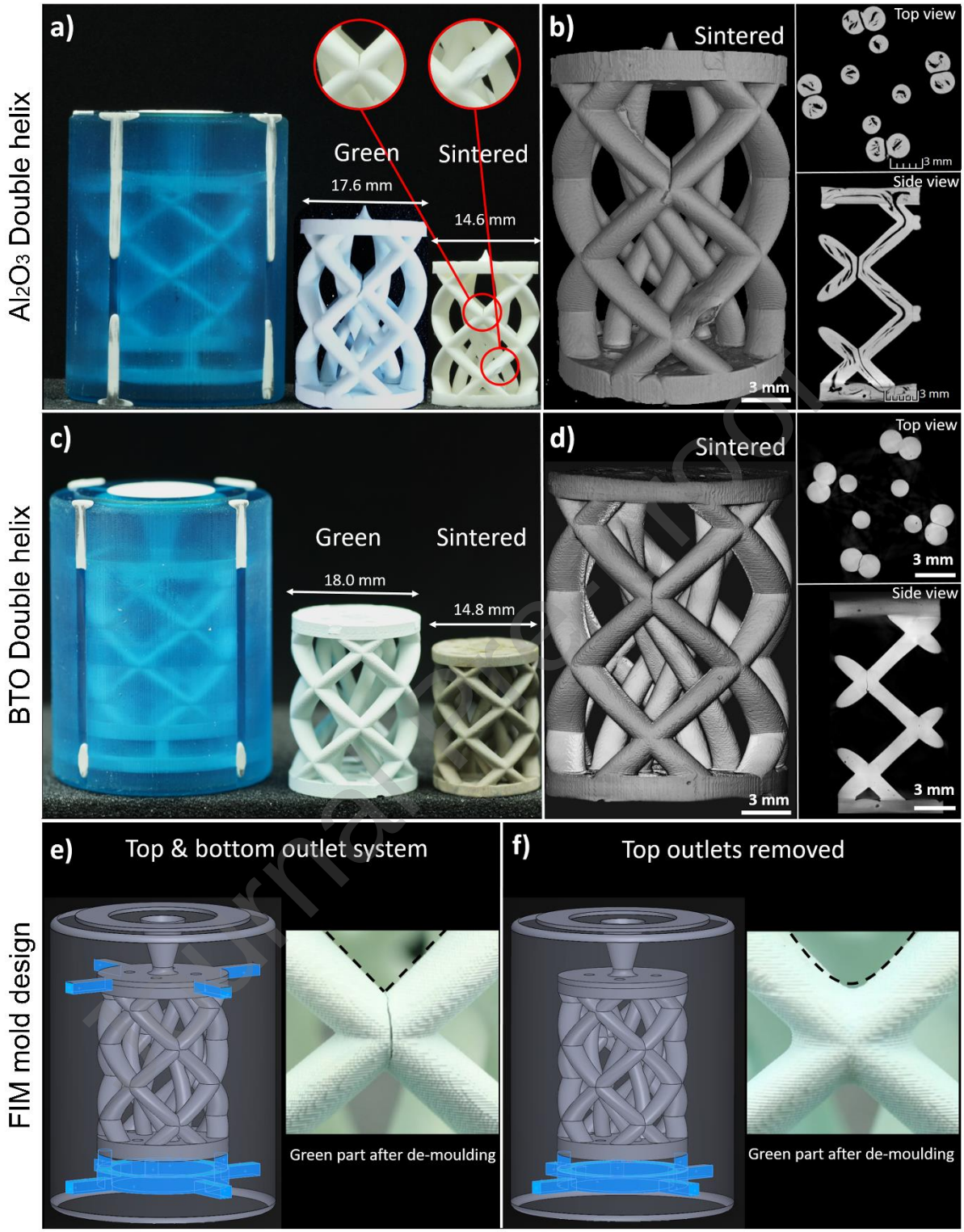

Fig. 4: a) Green and sintered Al_2O_3 double helix structures. b) The constructed volume from the CT scan for the sintered Al_2O_3 part and the defects shown in section views from the top and the side. c) Green and sintered $BaTiO_3$ double helix structures, d) Constructed volume from the CT scan for the sintered $BaTiO_3$ part and the section views as seen from the top and the side. e) The initial CAD model for the FIM mold with top outlets and the resulting crack after injection and de-molding magnified at the critical melt front junction. f) The updated CAD model with the top outlets removed and the resulting rounding on the green part magnified, where proper melt front fusion was achieved.

3.3 Densification and shape distortion

The densification and sintering of ceramics with 3D ceramic shapes can be complex. Issues like shape distortion generally arise from differential shrinkage in the materials due to constrained sintering conditions, residual stress from volumetric effects, and external forces, *e.g.,* gravity **[55, 56, 57, 58]**. Differential densification is also an important factor in defects **[59]**, hence can be used as a quality indicator.

The shrinkage and densification of the materials for the simple and complex shapes are summarized in **Fig. 5**. The plot collects the shrinkage from the green to the sintered state. The density of green and sintered geometries was measured on the fabricated parts by the Archimedes principle, depicted by the light grey and dark grey columns, respectively. The evolution of the shapes includes the dimensions at the CAD, those measured on the actual green parts and the CT scans of the sintered pieces. **Fig. 5a** highlights that the linear shrinkage from the green to the sintered parts ranged within 20% for the various shapes and materials. Such low values lead to fairly homogenous densification of simple and complex shapes. Both 3Y-TZP curved geometries obtained high densities, while the BNT-BT lens had a slightly lower density in the green and sintered state. A lower density of the Al_2O_3 double helix was measured due to the presence of voids and internal defects (**Fig. 3**). In contrast, improving the injection performance and the reduction of defects are in line with the higher density values of the BTO double helix.

Fig. 5b, c and **d** show the overlapping images of the three geometries "as-expected" at the CAD design with the sintered shape tomography to visualize the resulting shape distortion for the complex shapes. The as-expected volume (dark color) is derived from the CAD model and rescaled, assuming isotropic shrinkage in the piece, based on the actual measurements for calculating the linear shrinkage. These locations were the alignment points for the digital models to evaluate geometrical deviation on the entire structure. The largest deviation for the 3Y-TZP lens geometry (**Fig. 5b**) was observed on the edges of the bottom with +0.28 mm and +0.18 mm (green and yellow region). The negative deviation (dark regions) reached -0.07 mm and -0.05 mm (red labels) in two main regions with lower dimensions. The middle section exceeded up to +0.15 mm. A similar trend was also observed on the 3Y-TZP dome in **Fig. 5c**. The edges exhibited the largest deviations of +0.05 mm and +0.16 mm (shown in green). The middle section of the dome exhibits negative deviation values (dark color), with the maximum reaching -0.14 mm (red labels).

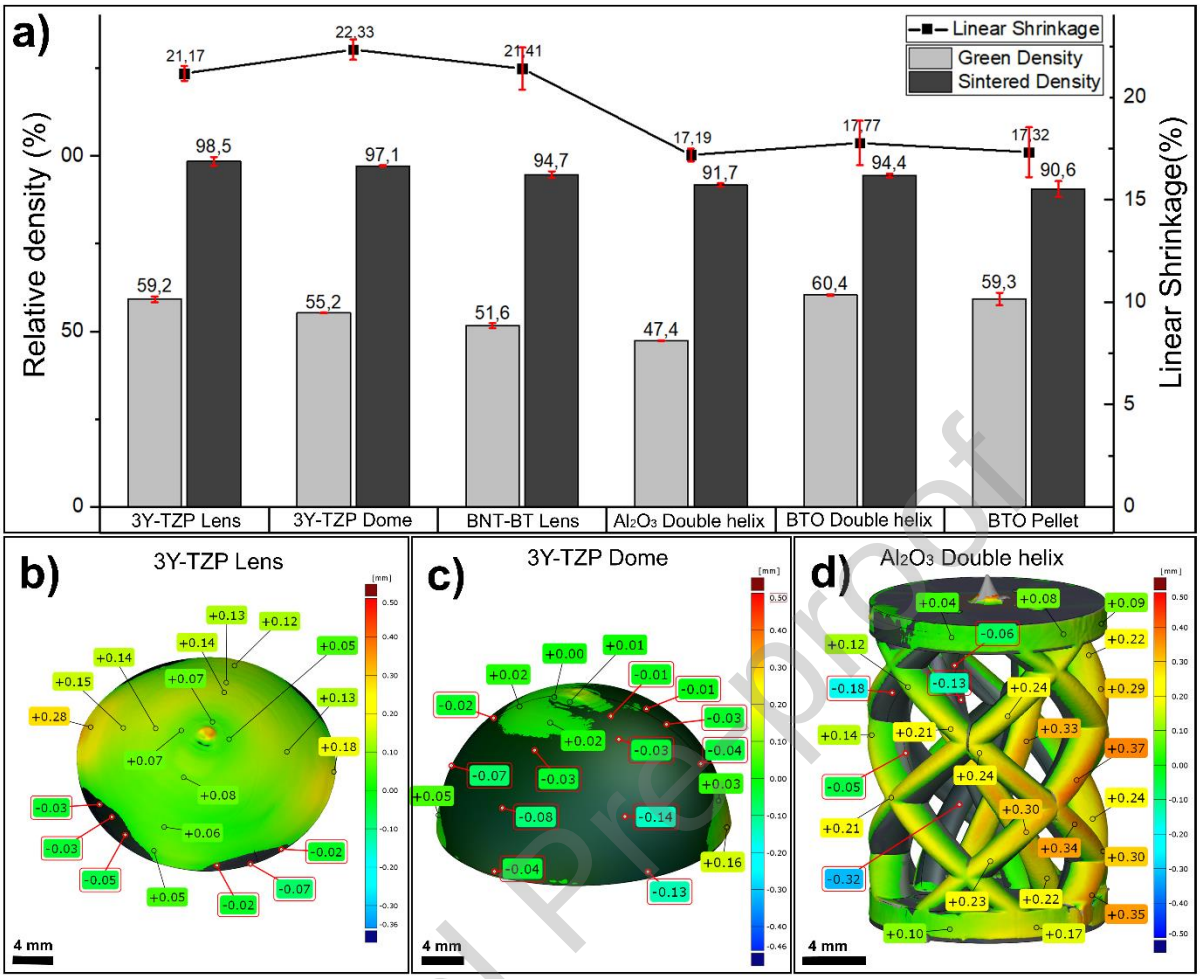

Fig. 5: a) The linear shrinkage calculated from the dimensions of sections on the green and sintered samples (line plot). The relative density of the green (in grey) and sintered (in black) geometries measured by the Archimedes principle. Geometrical deviation for the entire volume of the sintered parts fabricated, in respect to the measured linear shrinkage b) for the 3Y-TZP lens, c) the 3Y-TZP dome, and d) the Al_2O_3 double helix.

For the double helix in **Fig. 5d**, the alignment of the digital models revealed positive deviation (green/yellow regions), with the maximum values reaching +0.37 mm on the outer edges of the structure and other regions reaching +0.21 mm for the given alignment. The inner side of the structure deviates up to -0.32 mm and -0.18 mm (red labels), values comparable to the external deviations. The sintered part appears wider than the CAD model if uniform shrinkage was assumed for such complex geometry. For these larger geometries, the effect of gravity is also important as the geometries have a relatively low thickness for supporting the weight. Another important factor is the geometrical deviation resulting from injection molding, which could have resulted in larger dimensions on the green body transferred to the sintered parts. These results indicate that the shapes are relatively unchanged from the injection to the sintering.

Although densification could be challenging for some of the AM processes developed over the years, most recent lithography- and extrusion-based techniques allow the use of high solid loadings in the starting material and high sintered densities have been achieved **[14]**. Similarly, the FIM process with a comparable solid loading in the feedstock can yield high sintered densities. The non-directional nature of FIM eliminates interlayer defects that contribute to low density in AM.

The linear shrinkage of the commercial feedstocks was within the range specified on the material supplier datasheets. Therefore, the FIM process did not have an influence. The variation in relative density is attributed to the internal longitudinal defects (delaminations) found on the CT-Scan of the Al_2O_3 double helix compared to the BTO samples. Such defects that involve powder segregation **[60]** (and de-binding vapors) have been reported in conventional CIM. Feedstock freezing **[61]** could be magnified in FIM due to the different thermal properties of the thermoset mold compared to conventional metallic mold. However, increasing the injection pressure and temperature can reduce this effect, and defect-free samples can be produced (BTO double helix). The binder properties, in this case, were also important for the rheology and the green part strength. The mold design adjustment did not significantly affect the relative density, shrinkage or grain size, apart from alleviating (external) cracks on the critical points of the green structure.

3.4 Piezoelectric properties

Obtaining piezoelectric properties from printed piezoelectric ceramics is important for this hybrid process. Therefore, the electromechanical performance of the BTO experimental feedstock was evaluated in a cylindrical shape suitable for piezoelectric characterization, fabricated with the same injection parameters as the other shapes. The simple cylindrical shape of the pellet is commonly used in piezoelectric ceramics characterization, and it was selected to define a benchmark test where the geometry does not influence the electromechanical properties. **Fig. 6a** shows the room temperature ferro- and piezoelectric properties for BTO. The polarization-electric field behavior shows the ferroelectric hysteresis loop, with a coercive field at E_c= 0.613 kV/mm, remanent polarization at P_r = 7.9 μC/cm^2 and saturated polarization at P_s = 15.1 μC/cm^2, all in accordance with the expected behavior of BTO ceramics **[62]**. The strain-electric field curve exhibits the characteristic butterfly shape, with a maximum strain of 0.08% at an electric field of 2.6 kV/mm. After this measurement, the piezoelectric coefficient measured on a Berlincourt meter was d_{33}=35 pC/N. The sample was subsequently poled with an applied electric field of 2 kV/mm as it cooled down from elevated temperature (135°C) for approximately 3 hours until it reached room temperature. After the poling, the measured piezoelectric coefficient was d_{33}=120 pC/N. The values reported are

comparable with other studies found in the literature, with CIM and 3DP fabrication techniques, sintering temperatures and time, and poling parameters, as shown in **Table 2**.

The piezoelectric properties reported in the literature are often linked to the sintering conditions and resulting density/porosity. However, grain shape and domain wall movement are also important. The poling process contributes significantly to the piezoelectric properties despite the reduced density. Even low densities have yielded high d_{33} values when high electric fields or extended poling time have been used.

The non-uniform grain size in BTO is attributed to the sintering processes and related decomposition effects (such as Ba evaporation) at high temperatures. However, they are limited to the surface of the ceramic and do not substantially affect the final properties. The lower relative density in the case of the cylinder/pellet compared to the BTO double helix is a result of de-binding defects and filling defects originating from jetting phenomena **[63]**, which are common in CIM when the feedstock enters the cavity to fill relatively large and wide volumes for a given gate size. De-binding defects will reduce the density of sintered parts. However, they can also affect grain growth **[64]**, affecting porosity. Any defects can act as discontinuities in the bulk of the sample when the mechanical load is applied. However, the orientation of interlayer defects in AM repeated in the sample will have a greater influence **[65]**. In FIM, the lack of directionality in forming green structures is advantageous.

Table 2. Physical and piezoelectric properties of $BaTiO_3$ fabricated by different processes and thermal conditions.

Fabrication technique	**Sintering temperature & time**	**Relative density (%)**	**d_{33} (pC/N)**	**Strain (%)**	**Poling (Electric field, Temperature & Time)**	**Ref.**
FIM cylinder/pellet	1300°C for 4 h	90.6	120	0.08	2 kV/mm 130°C (20 min + cooling)	This work
Robocasting – Direct Ink Writing	1250 – 1350°C for 20 h	96	159	0.02	-	**[66]**
Micro- IM	1300°C for 2 h	-	-	-	-	**[67]**
Binder jetting	1260 – 1400°C for 5 h	65	13.2 – 74.1	-	0.2 kV/mm 120°C (2 h + cooling)	**[68]**
Binder jetting	1250°C for 6 h	36.7	113 -152.7	-	0.33 kV/mm 60°C (2 h)	**[65]**

Mask Image Projection-based Stereolithography	1330°C for 4-6 h	93.7	160	-	3 kV/mm 100°C (30 min)	**[69]**
Digital Light Processing	1330°C for 2 h	62.0 – 95.3	55.9 -168.1	-	2 kV/mm 60°C (15 min)	**[70]**
Digital Light Processing	1300 - 1330°C for 3 h	95.9 – 98.1	146 -206	-	5 kV/mm RT (30 min)	**[71]**
Digital Light Processing	1320°C for 2 h	95.4	180	-	3 kV/mm RT (15 min)	**[72]**
Stereolithography (SLA)	1300°C for 1 h	86 %	148	-	1.5 kV 120°C (15 m + cooling)	**[73]**
Paste extrusion	1300 - 1400°C for 4 h	65.3	128 -200	-	0.66 kV/mm 80°C (15 h)	**[74]**
Freeze-form Extrusion Fabrication	1250°C for 2 h	67.9 – 85.2	112 -204	-	0.54 kV/mm 90°C (2 h)	**[75]**
3DP – Paste extrusion (fine powder)	1300°C for 2-5-20 h	94	290-360-420	-	0.6 kV/mm 80°C (4 h + cooling)	**[76]**
Powder (Solid state – coprecipitation)	1330 – 1370°C for 2 – 4 h	93.9– 95.5	185- 260	-	2 kV/mm 110°C (min + cooling)	**[77]**

Curved samples were also extracted from the curved BNT-BT lens for electromechanical characterization (**Fig. 6e** and **f**). Polarization and strain *vs* electrical field are presented in **Fig. 6d**. The measurements display the characteristic ferroelectric hysteresis and butterfly loops. The coercive field was measured at E_c= 0.613 kV/mm with a spontaneous polarization at P_s = 30.4 μC/cm^2 and the remanent polarization at P_r = 26.0 μC/cm^2. The maximum stain recorded was 0.15 % (0.18 % for the negative field). The piezoelectric coefficient was d_{33}=104 pC/N, without any poling procedure applied in this case. The values for BNT-BT reported fall within the range reported in the literature for the different stoichiometries and electric fields applied **[78, 79]**.

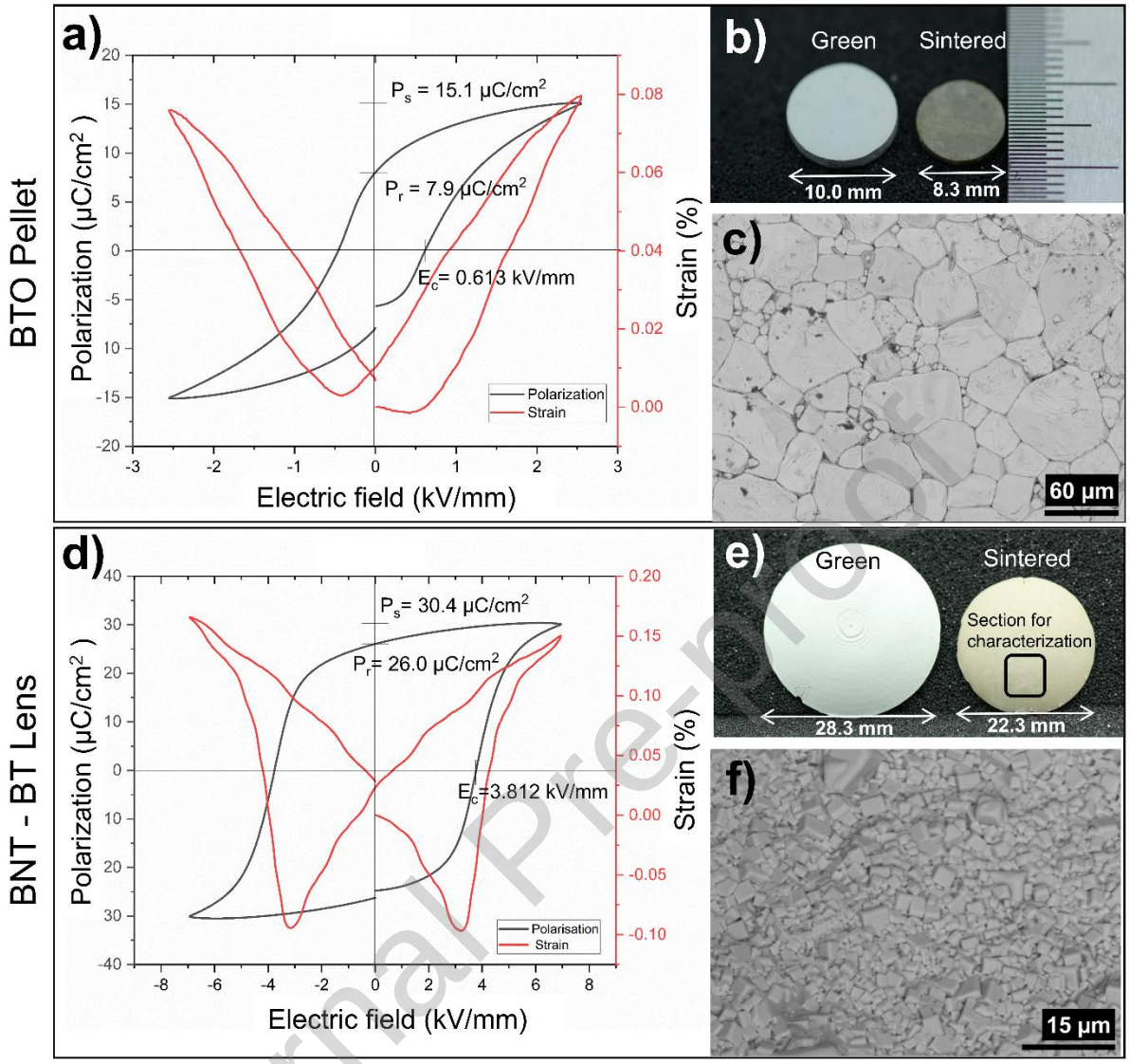

Fig. 6: The electromechanical performance of the piezoceramics. A) The polarization curve (in black) and the resulting strain (in red) of BTO cylinders/pellets during the piezoelectric measurement. b) The green and sintered parts used for the characterization. C) The BTO microstructure. D) The BNT-BT polarization curve (in black) and the resulting strain (in red). E) The section extracted from the sintered lens for the characterization. F) The BNT-BT microstructure.

In conclusion, the hybrid method expanded shape complexity and introduced experimental ceramic formulations that obtained functional properties. Geometry is not limited as long as electrodes can be properly placed on the object to avoid short-circuit paths between the positive and the negative electrode surfaces. The processing parameters, i.e., injection molding and sintering, are critical for defects and the resulting density, respectively, influencing the electromechanical performance. The combination of complex geometries and electromechanical performance offers great potential for advanced applications restricted by shape limitations or extensive material preparation stages.

4. Conclusion

A hybrid AM method based on Freeform Injection Molding (FIM) is demonstrated to feedstocks of several functional ceramic materials such as zirconia, alumina, and piezoceramics which can be challenging to print due to UV light scattering issues. Several simple and complex geometries were sintered successfully. The samples were free of the typical layered defects (delaminations and cracks) generally observed for other 3DP for ceramics, such as DLP, SLA and FDM. At the same time, the hybrid AM avoids inter-layer adhesion and anisotropic shrinkage issues. We demonstrate a few key strategies related to mold design and injection conditions to optimize the manufacturing process. A proper design of the gate and outlet positions in the FIM mold prevents the formation of weak points in the green state and reduces the cracks from mold expansion during dissolution. Proper control of melt front fusion in the feedstock during the injection is obtained by a facile tuning of temperature, pressure and the packing of the feedstock. We also adopted the full dissolution method for the more complex shapes, where the mold is fully dissolved, realizing the ceramic part. In this case, the green-ceramic strength strictly depends on the quality and design of the injection. For the sintering and consolidation of the ceramics, linear shrinkage was in line with the material specifications and literature, with a higher dimensional deviation measured for the piezoelectric ceramic-based feedstocks (BNT-BT and BTO). Simple and complex geometries exhibit isotropic shrinkage characteristics for the entire sintered volume. Shape distortion with excessive dimensional deviations was observed only on small regions located mainly on the edges and thinner parts. All the ceramic parts showed the expected grain growth and microstructures after sintering.

The electromechanical response of the piezoceramics (BNT-BT and BTO) proves that functionality is not restricted by the processing method and the geometries. Complex shapes combined with the electromechanical performance reported here are promising for advanced applications. The method is fast, versatile, and suitable for functional ceramics manufacturing.

Declaration of competing interest

The authors declare the following financial interests/personal relationships which may be considered as potential competing interests: K. Didilis, D. Marani and U. Bihlet are employees of Addifab ApS, where Freeform Injection Molding (FIM) was developed, manufacturer and supplier of the DLP printer and photopolymer resin used in this study. The authors declare no conflict of interest.

Acknowledgements

This work has received funding from Innovation Fund Denmark (IFD) in the framework of an Industrial PhD program [File No. 9065-00196B], VILLUM FONDEN [grant no. 37520] and the EU Horizon 2020 research and innovation program [grant No. 849119] for industrial research collaborations.

K. Didilis would like to acknowledge the support from Emil Meinild Christensen from the Danish Technological Institute (Denmark) for providing the 3Y-TZP CT scan data and Amandine Lorriaux from Safran Group (France) for providing the Al_2O_3 CT scan data. Axel Müller-Köhn from Fraunhofer IKTS (Germany) for compounding the BTO feedstock. Erling Ringgaard from Meggitt A/S (Denmark) for donating the BNT-BT powder.

REFERENCES

[1] D.S. Park, M. Hadad, L.M. Riemer, R. Ignatans, D. Spirito, V. Esposito, V. Tileli, N. Gauquelin, D. Chezganov, D. Jannis, J. Verbeeck, S. Gorfman, N. Pryds, P. Muralt, D. Damjanovic, Induced giant piezoelectricity in centrosymmetric oxides, Science (80). 375 (2022) 653–657. https://doi.org/10.1126/science.abm7497.

[2] J.K. Han, A. Kabir, V.B. Tinti, S. Santucci, D.S. Song, S.Y. Kim, W. Song, E. Kim, S.D. Bu, F. Kern, D.Z. De Florio, V. Esposito, Enhanced electromechanical properties in low-temperature gadolinium-doped ceria composites with low-dimensional carbon allotropes, J. Mater. Chem. A. 10 (2022) 4024–4031. https://doi.org/10.1039/d1ta10854a.

[3] V.B. Tinti, D. Marani, A. Kabir, A.B. Haugen, V. Esposito, D.Z. de Florio, Low-temperature synthesis of bismuth titanate by modified citrate amorphous method, Ceram. Int. 47 (2021) 12130–12136. https://doi.org/10.1016/j.ceramint.2021.01.058.

[4] C. Gadea, N. Phatharapeetranun, B. Ksapabutr, J.C. Grivel, V. Esposito, Stoichiometric control in $Bi_4Ti_3O_{12}$ synthesis by novel hybrid solid state reaction, Mater. Lett. 221 (2018) 101–103. https://doi.org/10.1016/j.matlet.2018.03.130.

[5] V. Esposito, C. Gadea, J. Hjelm, D. Marani, Q. Hu, K. Agersted, S. Ramousse, S.H. Jensen, Fabrication of thin yttria-stabilized-zirconia dense electrolyte layers by inkjet printing for high performing solid oxide fuel cells, J. Power Sources. 273 (2015) 89–95. https://doi.org/10.1016/j.jpowsour.2014.09.085.

[6] M.R. Sarker, S. Julai, M.F.M. Sabri, S.M. Said, M.M. Islam, M. Tahir, Review of piezoelectric energy harvesting system and application of optimization techniques to enhance the performance of the harvesting system, Sensors Actuators, A Phys. 300 (2019) 111634. https://doi.org/10.1016/j.sna.2019.111634.

[7] A.B. Haugen, A. Geffroy, A. Kaiser, V. Gil, MgO as a non-pyrolyzable pore former in porous membrane supports, J. Eur. Ceram. Soc. 38 (2018) 3279–3285. https://doi.org/10.1016/j.jeurceramsoc.2018.02.039.

[8] A.B. Haugen, J. Gurauskis, A. Kaiser, M. Søgaard, Graphite and PMMA as pore formers for thermoplastic extrusion of porous 3Y-TZP oxygen transport membrane supports, J. Eur. Ceram. Soc. 37 (2017) 1039–1047. https://doi.org/10.1016/j.jeurceramsoc.2016.10.001.

[9] P. Gonzalez, E. Schwarzer, U. Scheithauer, N. Kooijmans, T. Moritz, Additive manufacturing of functionally graded ceramic materials by stereolithography, J. Vis. Exp. 2019 (2019) 1–8. https://doi.org/10.3791/57943.

[10] K. Zhang, K. Wang, J. Chen, K. Wei, B. Liang, R. He, Design and additive manufacturing of 3D-architected ceramic metamaterials with programmable thermal expansion, Addit. Manuf. 47 (2021) 102338. https://doi.org/10.1016/j.addma.2021.102338.

[11] H. Wu, D. Li, Y. Tang, B. Sun, D. Xu, Rapid fabrication of alumina-based ceramic cores for gas turbine blades by stereolithography and gelcasting, J. Mater. Process. Technol. 209 (2009) 5886–5891. https://doi.org/10.1016/j.jmatprotec.2009.07.002.

[12] H.A. Rauch, H. Cui, K.P. Knight, R.J. Griffiths, J.K. Yoder, X. Zheng, H.Z. Yu, Additive manufacturing of yttrium-stabilized tetragonal zirconia: Progressive wall collapse, martensitic transformation, and energy dissipation in micro-honeycombs, Addit. Manuf. 52 (2022) 102692. https://doi.org/10.1016/j.addma.2022.102692.

[13] T. Moritz, A. Mannschatz, A. Müller-Köhn, A. Kucera, Current opportunities and challenges for CIM technology, CFI Ceram. Forum Int. 89 (2012) E21–E25.

[14] Y. Lakhdar, C. Tuck, J. Binner, A. Terry, R. Goodridge, Additive manufacturing of advanced ceramic materials, Prog. Mater. Sci. 116 (2021) 100736. https://doi.org/10.1016/j.pmatsci.2020.100736.

[15] E. Ferraris, J. Vleugels, Y. Guo, D. Bourell, J.P. Kruth, B. Lauwers, Shaping of engineering ceramics by electro, chemical and physical processes, CIRP Ann. – Manuf. Technol. 65 (2016) 761–784. https://doi.org/10.1016/j.cirp.2016.06.001.

[16] N. Travitzky, A. Bonet, B. Dermeik, T. Fey, I. Filbert-Demut, L. Schlier, T. Schlordt, P. Greil, Additive manufacturing of ceramic-based materials, Adv. Eng. Mater. 16 (2014) 729–754. https://doi.org/10.1002/adem.201400097.

[17] K. Hu, P. Zhao, J. Li, Z. Lu, High-resolution multiceramic additive manufacturing based on digital light processing, Addit. Manuf. 54 (2022) 102732. https://doi.org/10.1016/j.addma.2022.102732.

[18] J.C. Ruiz-Morales, A. Tarancón, J. Canales-Vázquez, J. Méndez-Ramos, L. Hernández-Afonso, P. Acosta-Mora, J.R. Marín Rueda, R. Fernández-González, Three dimensional printing of components and functional devices for energy and environmental applications, Energy Environ. Sci. 10 (2017) 846–859. https://doi.org/10.1039/c6ee03526d.

[19] A. Tarancon, V. Esposito, M.T. Faro, M. Di Vece, J.S. Son, P. Norby, S. Bag, P.S. Grant, A. Vogelpoth, S. Linnenbrink, M. Brucki, T. Schopphoven, A. Gasser, E. Persembe, D. Koufou, S. Kuhn, R. Ameloot, X. Hou, K. Engelbrecht, C.R.H. Bahl, N. Pryds, J. Wang, C. Tsouris, E. Miramontes, L. Love, C. Lai, X. Sun, M.R. Kærn, G. Criscuolo, D.B. Pedersen, 2022 Roadmap on 3D Printing for Energy, J. Phys. Energy. (2022). http://iopscience.iop.org/article/10.1088/2515-7655/ac483d.

[20] P. Qu, D. Xiong, Z. Zhu, Z. Gong, Y. Li, Y. Li, L. Fan, Z. Liu, P. Wang, C. Liu, Z. Chen, Inkjet printing additively manufactured multilayer SOFCs using high quality ceramic inks for performance enhancement, Addit. Manuf. 48 (2021) 102394. https://doi.org/10.1016/j.addma.2021.102394.

[21] O. Santoliquido, F. Camerota, A. Ortona, The influence of topology on DLP 3D printing, debinding and sintering of ceramic periodic architectures designed to replace bulky components, Open Ceram. 5 (2021) 100059. https://doi.org/10.1016/j.oceram.2021.100059.

[22] L. Lin, H. Wu, P. Ni, Y. Chen, Z. Huang, Y. Li, K. Lin, P. Sheng, S. Wu, Additive manufacturing of complex-shaped and high-performance aluminum nitride-based components for thermal management, Addit. Manuf. 52 (2022) 102671. https://doi.org/10.1016/j.addma.2022.102671.

[23] J. Rauchenecker, J. Rabitsch, M. Schwentenwein, T. Konegger, Additive manufacturing of aluminum nitride ceramics with high thermal conductivity via digital light processing, Open Ceram. 9 (2022) 100215. https://doi.org/10.1016/j.oceram.2021.100215.

[24] J. Guo, Y. Zeng, P. Li, J. Chen, Fine lattice structural titanium dioxide ceramic produced by DLP 3D printing, Ceram. Int. 45 (2019) 23007–23012. https://doi.org/10.1016/j.ceramint.2019.07.346.

[25] F. Wang, Z. Li, Y. Lou, F. Zeng, M. Hao, W. Lei, X. Wang, X. Wang, G. Fan, W. Lu, Stereolithographic additive manufacturing of Luneburg lens using Al_2O_3-based low sintering temperature ceramics for 5G MIMO antenna, Addit. Manuf. 47 (2021) 102244. https://doi.org/10.1016/j.addma.2021.102244.

[26] H. Cui, R. Hensleigh, D. Yao, D. Maurya, P. Kumar, M.G. Kang, S. Priya, X. (Rayne) Zheng, Three-dimensional printing of piezoelectric materials with designed anisotropy and directional response, Nat. Mater. 18 (2019) 234–241. https://doi.org/10.1038/s41563-018-0268-1.

[27] W. Wang, J. Sun, B. Guo, X. Chen, K.P. Ananth, J. Bai, Fabrication of piezoelectric nano-ceramics via stereolithography of low viscous and non-aqueous suspensions, J. Eur. Ceram. Soc. 40 (2020) 682–688. https://doi.org/10.1016/j.jeurceramsoc.2019.10.033.

[28] J.W. Halloran, Ceramic Stereolithography: Additive Manufacturing for Ceramics by Photopolymerization, Annu. Rev. Mater. Res. 46 (2016) 19–40. https://doi.org/10.1146/annurev-matsci-070115-031841.

[29] C.J. Bae, J.W. Halloran, Concentrated suspension-based additive manufacturing – viscosity, packing density, and segregation, J. Eur. Ceram. Soc. 39 (2019) 4299–4306. https://doi.org/10.1016/j.jeurceramsoc.2019.05.034.

[30] F. Qi, N. Chen, Q. Wang, Preparation of PA11/$BaTiO_3$ nanocomposite powders with improved processability, dielectric and piezoelectric properties for use in selective laser sintering, Mater. Des. 131 (2017) 135–143. https://doi.org/10.1016/j.matdes.2017.06.012.

[31] Z. Chen, Z. Li, J. Li, C. Liu, C. Lao, Y. Fu, C. Liu, Y. Li, P. Wang, Y. He, 3D printing of ceramics: A review, J. Eur. Ceram. Soc. 39 (2019) 661–687. https://doi.org/10.1016/j.jeurceramsoc.2018.11.013.

[32] Z. Chen, X. Sun, Y. Shang, K. Xiong, Z. Xu, R. Guo, S. Cai, C. Zheng, Dense ceramics with complex shape fabricated by 3D printing: A review, J. Adv. Ceram. 10 (2021) 195–218. https://doi.org/10.1007/s40145-020-0444-z.

[33] M. Rosa, C. Barou, V. Esposito, Zirconia UV-curable colloids for additive manufacturing via hybrid inkjet printing-stereolithography, Mater. Lett. 215 (2018) 214–217. https://doi.org/10.1016/j.matlet.2017.12.096.

[34] M. Rosa, P.N. Gooden, S. Butterworth, P. Zielke, R. Kiebach, Y. Xu, C. Gadea, V. Esposito, Zirconia nano-colloids transfer from continuous hydrothermal synthesis to inkjet printing, J. Eur. Ceram. Soc. 39 (2019) 2–8. https://doi.org/10.1016/j.jeurceramsoc.2017.11.035.

[35] H. Wu, D. Li, Y. Tang, B. Sun, D. Xu, Rapid fabrication of alumina-based ceramic cores for gas turbine blades by stereolithography and gelcasting, J. Mater. Process. Technol. 209 (2009) 5886–5891. https://doi.org/10.1016/j.jmatprotec.2009.07.002.

[36] R. Liska, F. Schwager, C. Maier, R. Cano-Vives, J. Stampfl, Water-soluble photopolymers for rapid prototyping of cellular materials, J. Appl. Polym. Sci. 97 (2005) 2286–2298. https://doi.org/10.1002/app.22025.

[37] J. Stampfl, A. Wöß, S. Seidler, H. Fouad, A. Pisaipan, F. Schwager, R. Liska, Water soluble, photocurable resins for rapid prototyping applications, in: Macromol. Symp., John Wiley and Sons Ltd, 2004: pp. 99–108. https://doi.org/10.1002/masy.200451308.

[38] R. Lu, S. Chandrasekaran, W.L. Du Frane, R.L. Landingham, M.A. Worsley, J.D. Kuntz, Complex shaped boron carbides from negative additive manufacturing, Mater. Des. 148 (2018) 8–16. https://doi.org/10.1016/j.matdes.2018.03.026.

[39] S. Peng, Z. Wang, J. Lin, J.T. Miao, L. Zheng, Z. Yang, Z. Weng, L. Wu, Tailored and Highly Stretchable Sensor Prepared by Crosslinking an Enhanced 3D Printed UV-Curable Sacrificial Mold, Adv. Funct. Mater. 31 (2021) 1–9. https://doi.org/10.1002/adfm.202008729.

[40] S. Aabith, R. Caulfield, O. Akhlaghi, A. Papadopoulou, 3D direct-write printing of water soluble micromoulds for high-resolution rapid prototyping, Addit. Manuf. 58 (2022) 103019. https://doi.org/10.1016/j.addma.2022.103019.

[41] M. Alsharari, B. Chen, W. Shu, Sacrificial 3D Printing of Highly Porous, Soft Pressure Sensors, Adv. Electron. Mater. 8 (2022) 1–12. https://doi.org/10.1002/aelm.202100597.

[42] E. Sharifi, A. Chaudhuri, B.V. Waehrens, L.G. Staal, S.D. Farahani, Assessing the suitability of freeform injection molding for low volume injection molded parts: A design science approach, Sustain. 13 (2021) 1–19. https://doi.org/10.3390/su13031313.

[43] E. Sharifi, A. Chaudhuri, B.V. Wæhrens, L.G. Staal, S.D. Farahani, Part Selection for Freeform Injection Molding: Framework for Development of a Unique Methodology, IFIP Adv. Inf. Commun. Technol., Springer, 2020: pp. 723–730. https://doi.org/10.1007/978-3-030-57997-5_83.

[44] A. Basso, M. Mendez Ribo, A. Halina Danielak, B. Yang, P. Kjeldsteen, P. Valler, D. Bue Pedersen, Y. Zhang, 3d Printed Mold for Powder Injection Molding Process, in: Adv. Precis. Addit. Manuf., 2019. www.euspen.eu.

[45] A. Müller-köhn, E. Schwarzer, K. Didilis, U. Bihlet, T. Moritz, 3D-printed single-use polymer moulds for Prototypes and Small Series suitable for Powder Injection Moulding, in: Euro PM2020 - MIM Adv. Process., 2020.

[46] U. Bihlet, K. Didilis, P. Grimmer, M. Geisler, Rapid tooling development with freeform injection molding for MIM, in: 2021 Int. Conf. Powder Metall. Part. Mater. PowderMet 2021, Metal Powder Industries Federation, 2021: pp. 143–149.

[47] R. Wick-Joliat, M. Tschamper, R. Kontic, D. Penner, Water-soluble sacrificial 3D printed molds for fast prototyping in ceramic injection molding, Addit. Manuf. 48 (2021) 102408. https://doi.org/10.1016/j.addma.2021.102408.

[48] K. Didilis, U. Bihlet, A. Lorriaux, A. Agne, Compatibility of CIM feedstocks with 3D-printed single-use polymer molds, in: Proc. 2021 Int. Conf. Powder Metall. Part. Mater., Metal Powder Industries Federation, 2021: pp. 150–157.

[49] C.A. Schneider, W.S. Rasband, K.W. Eliceiri, NIH Image to ImageJ: 25 years of image analysis, Nat. Methods. 9 (2012) 671–675. https://doi.org/10.1038/nmeth.2089.

[50] W.J. Tseng, C.-K. Hsu, Cracking defect and porosity evolution during thermal debinding in ceramic injection moldings, n.d.

[51] S. Krug, J.R.G. Evans, J.H.H. Ter Maat, Residual stresses and cracking in large ceramic injection mouldings subjected to different solidification schedules, J. Eur. Ceram. Soc. 20 (2000) 2535–2541. https://doi.org/10.1016/S0955-2219(00)00120-5.

[52] F. Raether, A. Klimera, Methods of measurement and strategies for binder removal in ceramics, CFI Ceram. Forum Int. 85 (2008) 5–11.

[53] L. Deng, L. Qiao, J. Zheng, Y. Ying, J. Yu, W. Li, S. Che, W. Cai, Injection molding, debinding and sintering of ZrO_2 ceramic modified by silane couping agent, J. Eur. Ceram. Soc. 40 (2020) 1566–1573. https://doi.org/10.1016/j.jeurceramsoc.2019.11.069.

[54] M. Trunec, Effect of grain size on mechanical properties of 3Y-TZP ceramics, Ceram. – Silikaty. 52 (2008) 165–171.

[55] J.A. Glasscock, V. Esposito, S.P.V. Foghmoes, T. Stegk, D. Matuschek, M.W.H. Ley, S. Ramousse, The effect of forming stresses on the sintering of ultra-fine $Ce_{0.9}Gd_{0.1}O_{2-\delta}$ powders, J. Eur. Ceram. Soc. 33 (2013) 1289–1296. https://doi.org/10.1016/j.jeurceramsoc.2012.12.015.

[56] F. Teocoli, D.W. Ni, K. Brodersen, S.P.V. Foghmoes, S. Ramousse, V. Esposito, Effects of co-sintering in self-standing CGO/YSZ and CGO/ScYSZ dense bi-layers, J. Mater. Sci. 49 (2014) 5324–5333. https://doi.org/10.1007/s10853-014-8235-y.

[57] H.L. Frandsen, E. Olevsky, T.T. Molla, V. Esposito, R. Bjørk, N. Pryds, Modeling sintering of multilayers under influence of gravity, J. Am. Ceram. Soc. 96 (2013) 80–89. https://doi.org/10.1111/jace.12070.

[58] E. Olevsky, T.T. Molla, H.L. Frandsen, R. Bjørk, V. Esposito, D.W. Ni, A. Ilyina, N. Pryds, Sintering of multilayered porous structures: Part I-constitutive models, J. Am. Ceram. Soc. 96 (2013) 2657–2665. https://doi.org/10.1111/jace.12375.

[59] D.J. Green, O. Guillon, J. Rödel, Constrained sintering: A delicate balance of scales, J. Eur. Ceram. Soc. 28 (2008) 1451–1466. https://doi.org/10.1016/j.jeurceramsoc.2007.12.012.

[60] A. Greiner, D. Kauzlarić, J.G. Korvink, R. Heldele, M. Schulz, V. Piotter, T. Hanemann, O. Weber, J. Haußelt, Simulation of micro powder injection moulding: Powder segregation and yield stress effects during form filling, J. Eur. Ceram. Soc. 31 (2011) 2525–2534. https://doi.org/10.1016/j.jeurceramsoc.2011.02.008.

[61] A. Mannschatz, A. Müller, T. Moritz, Influence of powder morphology on properties of ceramic injection moulding feedstocks, J. Eur. Ceram. Soc. 31 (2011) 2551–2558. https://doi.org/10.1016/j.jeurceramsoc.2011.01.013.

[62] B. Jaffe, W.R. Cook, H. Jaffe, Piezoelectric Ceramics, 1st ed., Academic Press, 1971. https://doi.org/https://doi.org/10.1016/B978-0-12-379550-2.X5001-7.

[63] P. Dvorak, T. Barriere, J.C. Gelin, Direct observation of mould cavity filling in ceramic injection moulding, J. Eur. Ceram. Soc. 28 (2008) 1923–1929. https://doi.org/10.1016/j.jeurceramsoc.2008.02.001.

[64] K. Liu, C. Zhou, J. Hu, S. Zhang, Q. Zhang, C. Sun, Y. Shi, H. Sun, C. Yin, Y. Zhang, Y. Fu, Fabrication of barium titanate ceramics via digital light processing 3D printing by using high refractive index monomer, J. Eur. Ceram. Soc. 41 (2021) 5909–5917. https://doi.org/10.1016/j.jeurceramsoc.2021.04.044.

[65] L.A. Chavez, B.R. Wilburn, P. Ibave, L.C. Delfin, S. Vargas, H. Diaz, C. Fulgentes, A. Renteria, J. Regis, Y. Liu, R.B. Wicker, Y. Lin, Fabrication and characterization of 3D printing induced orthotropic functional ceramics, Smart Mater. Struct. 28 (2019). https://doi.org/10.1088/1361-665X/ab4e0a.

[66] C. Gadea, T. Spelta, S.B. Simonsen, V. Esposito, J.R. Bowen, A.B. Haugen, Hybrid inks for 3D printing of tall $BaTiO_3$-based ceramics, Open Ceram. 6 (2021) 100110. https://doi.org/10.1016/j.oceram.2021.100110.

[67] V. Onbattuvelli, R.K. Enneti, S.-B. Sohn, T. Mccabe, S.-J. Park, S. re, Micro-powder injection moulding of barium titanate, Powder Inject. Mould. Int. 59 (2011).

[68] S.M. Gaytan, M.A. Cadena, H. Karim, D. Delfin, Y. Lin, D. Espalin, E. MacDonald, R.B. Wicker, Fabrication of barium titanate by binder jetting additive manufacturing technology, Ceram. Int. 41 (2015) 6610–6619. https://doi.org/10.1016/j.ceramint.2015.01.108.

[69] Z. Chen, X. Song, L. Lei, X. Chen, C. Fei, C. Tat, X. Qian, T. Ma, Y. Yang, K. Shung, Y. Chen, Q. Zhou, Nano Energy 3D printing of piezoelectric element for energy focusing and ultrasonic sensing, Nano Energy. 27 (2016) 78–86. https://doi.org/10.1016/j.nanoen.2016.06.048.

[70] K. Liu, C. Zhou, J. Hu, S. Zhang, Q. Zhang, C. Sun, Y. Shi, H. Sun, C. Yin, Y. Zhang, Y. Fu, Fabrication of barium titanate ceramics via digital light processing 3D printing by using high refractive index monomer, J. Eur. Ceram. Soc. 41 (2021) 5909–5917. https://doi.org/10.1016/j.jeurceramsoc.2021.04.044.

[71] X. Chen, J. Sun, B. Guo, Y. Wang, S. Yu, W. Wang, J. Bai, Effect of the particle size on the performance of $BaTiO_3$ piezoelectric ceramics produced by additive manufacturing, Ceram. Int. 48 (2022) 1285–1292. https://doi.org/10.1016/j.ceramint.2021.09.213.

[72] C.L. Liu, Q. Du, C. Zhang, J.M. Wu, G. Zhang, Y.S. Shi, Fabrication and properties of $BaTiO_3$ ceramics via digital light processing for piezoelectric energy harvesters, Addit. Manuf. 56 (2022) 102940. https://doi.org/10.1016/j.addma.2022.102940.

[73] A. Smirnov, S. Chugunov, A. Kholodkova, M. Isachenkov, A. Tikhonov, O. Dubinin, I. Shishkovsky, The Fabrication and Characterization of $BaTiO_3$ Piezoceramics Using SLA 3D Printing at 465 nm Wavelength, Materials (Basel). 15 (2022). https://doi.org/10.3390/ma15030960.

[74] H.K.A. Renteria-marquez, N.D. Love, Y. Lin, D. Islam, L.A. Chavez, Fabrication of bulk piezoelectric and dielectric $BaTiO_3$ ceramics using paste extrusion 3D printing technique, (2019) 3685–3694. https://doi.org/10.1111/jace.16242.

[75] A. Renteria, J.A. Diaz, B. He, I.A. Renteria-Marquez, L.A. Chavez, J.E. Regis, Y. Liu, D. Espalin, T.L. Tseng, Y. Lin, Particle size influence on material properties of $BaTiO_3$ ceramics fabricated using freeze-form extrusion 3D printing, Mater. Res. Express. 6 (2019). https://doi.org/10.1088/2053-1591/ab4a36.

[76] X. Wei, Y. Liu, D. Zhao, S.S. Ge, 3D printing of piezoelectric barium titanate with high density from milled powders, J. Eur. Ceram. Soc. 40 (2020) 5423–5430. https://doi.org/10.1016/j.jeurceramsoc.2020.06.021.

[77] L. Simon-Seveyrat, A. Hajjaji, Y. Emziane, B. Guiffard, D. Guyomar, Re-investigation of synthesis of $BaTiO_3$ by conventional solid-state reaction and oxalate coprecipitation route for piezoelectric applications, Ceram. Int. 33 (2007) 35–40. https://doi.org/10.1016/j.ceramint.2005.07.019.

[78] S. Mhin, J. Lee, J.H. Ryu, Processing, structure, and properties of lead-free piezoelectric NBT-BT, J. Korean Cryst. Growth Cryst. Technol. 25 (2015) 160–165. https://doi.org/10.6111/JKCGCT.2015.25.4.160.

[79] L.M. Denis, J. Glaum, M. Hoffman, J.E. Daniels, R.J. Hooper, G. Tutuncu, J.S. Forrester, J.L. Jones, Effect of mechanical depoling on piezoelectric properties of $Na_{0.5}Bi_{0.5}TiO_3$–$xBaTiO_3$ in the morphotropic phase boundary region, J. Mater. Sci. 53 (2018) 1672–1679. https://doi.org/10.1007/s10853-017-1616-2.

List of Figures

measurement. b) The green and sintered parts used for the characterization. c) The BTO microstructure. d) The BNT-BT polarization curve (in black) and the resulting strain (in red). e) The section extracted from the sintered lens for the characterization. f) The BNT-BT microstructure. 19

List of Tables

Author statement

Kyriakos Didilis: Conceptualization, Data curation, Investigation, Methodology, Visualization, Writing – original draft, Writing – review & editing

Debora Marani: Supervision, Writing – original draft, Writing – review & editing

Uffe Bihlet: Funding acquisition, Project administration, Supervision

Astri Bjørnetun Haugen: Data curation, Funding acquisition, Supervision, Writing – original draft, Writing – review & editing

Vincenzo Esposito: Conceptualization, Data curation, Funding acquisition, Project administration, Supervision, Writing – original draft, Writing – review & editing

Declaration of interests

☐ The authors declare that they have no known competing financial interests or personal relationships that could have appeared to influence the work reported in this paper.

☒ The authors declare the following financial interests/personal relationships which may be considered as potential competing interests:

Kyriakos Didilis reports financial support was provided for this Industrial Ph.D. project by Innovation Fund Denmark [File No. 9065-00196B], VILLUM FONDEN [grant no. 37520], and EU Horizon 2020 [grant No. 849119]. Kyriakos Didilis, Debora Marani, and Uffe Bihlet report a relationship with Addifab ApS that include: employment.

Highlights

- Hybrid additive manufacturing and injection molding produce 3D complex shapes
- 3D-printed sacrificial molds allow molding the ceramics in freeform geometries
- Photopolymer formulation results in robust printing and injection performance
- Strategy to reduce defects by simulations and to adjust injection molding parameters
- Sintered parts show isotropic shrinkage, no delaminations and limited shape distortion
- 3D Pb-free piezoceramics preserve their piezoelectric properties